Properties of Kilonovae from Dynamical and Post-merger Ejecta of Neutron Star Mergers

Draft version December 17, 2021
Preprint typeset using LaTeX style emulateapj v. 12/16/11

PROPERTIES OF KILONOVAE FROM DYNAMICAL AND POST-MERGER EJECTA OF NEUTRON STAR MERGERS

Masaomi Tanaka[1], Daiji Kato[2,3,4], Gediminas Gaigalas[5], Pavel Rynkun[5], Laima Radžiūtė[5], Shinya Wanajo[6,7], Yuichiro Sekiguchi[8], Nobuyuki Nakamura[9], Hajime Tanuma[10], Izumi Murakami[2,3], Hiroyuki A. Sakaue[2]

Draft version December 17, 2021

ABSTRACT

Ejected material from neutron star mergers give rise to electromagnetic emission powered by radioactive decays of r-process nuclei, which is so called kilonova or macronova. While properties of the emission are largely affected by opacities in the ejected material, available atomic data for r-process elements are still limited. We perform atomic structure calculations for r-process elements: Se ($Z = 34$), Ru ($Z = 44$), Te ($Z = 52$), Ba ($Z = 56$), Nd ($Z = 60$), and Er ($Z = 68$). We confirm that the opacities from bound-bound transitions of open f-shell, Lanthanide elements (Nd and Er) are higher than those of the other elements over a wide wavelength range. The opacities of open s-shell (Ba), p-shell (Se and Te), and d-shell (Ru) elements are lower than those of open f-shell elements and their transitions are concentrated in the ultraviolet wavelengths. We show that the optical brightness can be different by > 2 mag depending on the element abundances in the ejecta such that post-merger, Lanthanide-free ejecta produce brighter and bluer optical emission. Such blue emission from post-merger ejecta can be observed from the polar directions if the mass of the preceding dynamical ejecta in these regions is small. For the ejecta mass of 0.01 $M_\odot$, observed magnitudes of the blue emission will reach 21.0 mag (100 Mpc) and 22.5 mag (200 Mpc) in g and r bands within a few days after the merger, which are detectable with 1m or 2m-class telescopes.

Keywords: gravitational waves — radiative transfer — opacity — nuclear reactions, nucleosynthesis, abundances — stars: neutron

1. INTRODUCTION

Direct detection of gravitational waves (GW) opened the era of GW astronomy (Abbott et al. 2016c,a, 2017). A next important step will be an identification of their electromagnetic (EM) counterparts to further study the astrophysical nature of the GW sources, as sky localization by GW detectors is not accurate enough to pin down their positions (Abbott et al. 2016d). In fact, extensive EM follow-up observations have been performed for the detected GW events so far (Abbott et al. 2016b).

From compact binary mergers including at least one neutron star (NS), i.e., NS-NS mergers and black hole (BH)-NS mergers, various EM signals are expected over a wide wavelength range (e.g., Metzger & Berger 2012; Rosswog 2015). One of the most promising EM transients is so called "kilonova" or "macronova", which is the emission powered by the radioactive decays of newly synthesized r-process nuclei (Li & Paczyński 1998; Kulkarni 2005; Metzger et al. 2010). For recent reviews of kilonova emission, see Fernández & Metzger (2016), Tanaka (2016), and Metzger (2017). Kilonova emission is a good candidate for optical and near infrared follow-up observations after the detection of GWs (Smartt et al. 2016; Soares-Santos et al. 2016; Kasliwal et al. 2016; Morokuma et al. 2016; Cowperthwaite et al. 2016; Yoshida et al. 2017).

Kilonova emission from the dynamical ejecta ($\sim 10^{-3}$–$10^{-2} M_\odot$) of neutron star mergers is likely to have a luminosity of $\sim 10^{40} - 10^{41}$ erg s^{-1} with a timescale of about 1 week, which is expected to peak at red optical or near-infrared wavelengths (Kasen et al. 2013; Barnes & Kasen 2013; Tanaka & Hotokezaka 2013). This is due to the high opacities of r-process elements in the ejecta, especially those of Lanthanide elements (Kasen et al. 2013). In fact, short GRB 130603B showed an near-infrared excess in the afterglow (Tanvir et al. 2013; Berger et al. 2013), which was interpreted as a kilonova signal (see also Hotokezaka et al. 2013b; Piran et al. 2014). In addition, possible kilonova candidates have been reported for GRB 060614 (Yang et al. 2015; Jin et al. 2015) and GRB 050709 (Jin et al. 2016).

After the dynamical mass ejection, NS-NS mergers and BH-NS mergers are expected to have further mass ejection by viscous heating (Dessart et al. 2009; Fernández & Metzger 2013; Fernández et al. 2015a,b; Shibata et al. 2017) that originates from magnetohydrodynamic turbulence (Price & Rosswog 2006; Kiuchi et al. 2014, 2015; Giacomazzo et al. 2015; Ciolfi et al. 2017; Siegel & Metzger 2017), and subdominantly by neutrino heating (Wanajo

[1] National Astronomical Observatory of Japan, Osawa, Mitaka, Tokyo 181-8588, Japan; masaomi.tanaka@nao.ac.jp
[2] National Institute for Fusion Science, Oroshi-cho, Toki, Gifu 509-5292, Japan
[3] Department of Fusion Science, SOKENDAI, Oroshi-cho, Toki, Gifu 509-5292, Japan
[4] Department of Advanced Energy Engineering, Kyushu University, Kasuga, Fukuoka 816-8580, Japan
[5] Institute of Theoretical Physics and Astronomy, Vilnius University, Saulėtekio av. 3, LT-10257 Vilnius, Lithuania
[6] Department of Engineering and Applied Sciences, Sophia University, Chiyoda-ku, Tokyo 102-8554, Japan
[7] RIKEN, iTHES Research Group, 2-1 Hirosawa, Wako, Saitama 351-0198, Japan
[8] Department of Physics, Toho University, Funabashi, Chiba 274-8510, Japan
[9] Institute for Laser Science, The University of Electro-Communications, Chofugaoka, Chofu Tokyo 182-8585, Japan
[10] Department of Physics, Tokyo Metropolitan University, Minami-Osawa, Hachioji, Tokyo 192-0397, Japan

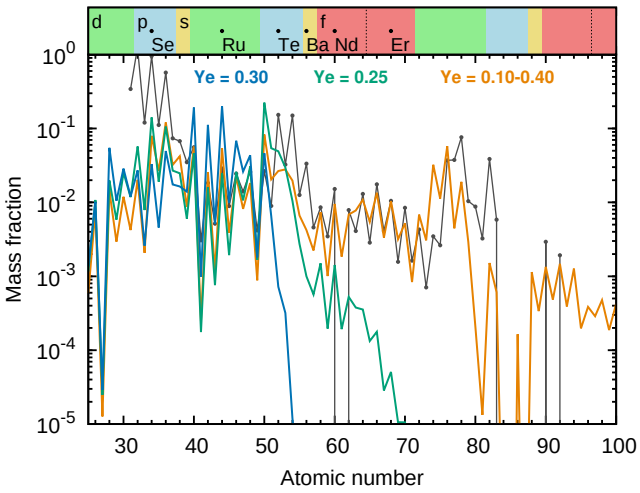

Figure 1. Element abundances in the ejecta of NS mergers at $t = 1$ day after the merger. The orange line shows abundances for dynamical ejecta (Wanajo et al. 2014), which is derived by averaging the nucleosynthesis results of $Y_e = 0.10 - 0.40$ assuming a flat Y_e distribution. The blue and green lines show the nucleosynthesis results from trajectories of $Y_e = 0.25$ and 0.30, respectively, which represent the abundance patterns of high-Y_e post-merger ejecta. Black points connected with the line show the solar abundance ratios of r-process elements (Simmerer et al. 2004).

& Janka 2012; Perego et al. 2014; Fujibayashi et al. 2017) and nuclear recombination (Fernández & Metzger 2013). These components are as a whole denoted as "post-merger" ejecta in this paper. The post-merger ejecta can consist of less neutron rich material than in the dynamical ejecta (Just et al. 2015; Martin et al. 2015; Wu et al. 2016; Lippuner et al. 2017); neutrino absorption as well as a high temperature caused by viscous heating makes ejected material less neutron rich or electron fraction Y_e (number of protons per nucleon) higher. If the ejecta are free from Lanthanide elements, the emission from post-merger ejecta can be brighter and bluer, which can be called "blue kilonova" (Metzger & Fernández 2014; Kasen et al. 2015). However, due to the lack of atomic data of r-process elements, previous studies assume opacities of Fe for Lanthanide-free ejecta. To predict emission properties of kilonova, systematic atomic data for r-process elements are important (see Kasen et al. 2013; Fontes et al. 2017; Wollaeger et al. 2017).

In this paper, we newly perform atomic structure calculations for selected r-process elements. Using these data, we perform radiative transfer simulations and study the impact of element abundances to kilonova emission. In Section 2, we show methods and results of our atomic structure calculations. In Section 3, we calculate opacities with these atomic data and discuss the dependence on the elements. We then apply our data for radiative transfer simulations in Section 4, and show light curves of kilonova from dynamical and post-merger ejecta of NS mergers. Finally we give summary in Section 5.

2. ATOMIC STRUCTURE CALCULATIONS

We perform atomic structure calculations for Se ($Z = 34$), Ru ($Z = 44$), Te ($Z = 52$), Ba ($Z = 56$), Nd ($Z = 60$) and Er ($Z = 68$). These elements are selected to systematically study the opacities of elements with different open shells: Ba is an open s-shell element, Se and Te are open p-shell elements, Ru is an open d-shell element, and Nd and Er are open f-shell elements. We focus on neutral atom and singly and doubly ionized ions because these ionization states are most common in kilonova at $t \gtrsim 1$ day after the merger (Kasen et al. 2013; Tanaka & Hotokezaka 2013).

In Figure 1, these elements are shown with three different abundance patterns in the ejecta of NS mergers. While relativistic simulations of NS mergers predict wide ranges of Y_e between 0.05 and 0.45, the detailed Y_e distributions depend on the NS masses and their ratios as well as the adopted nuclear equations of state (Sekiguchi et al. 2015, 2016). In this paper, we assume a flat mass distribution between $Y_e = 0.10$ and 0.40 as representative of dynamical ejecta. As shown in Figure 1 (orange line), the dynamical ejecta consist of a wide range of r-process elements from the first ($Z = 34$) to third ($Z = 78$) abundance peaks. For the post-merger ejecta, we consider single Y_e models of 0.25 (green) and 0.30 (blue) for simplicity. The former represents a case that contains the second ($Z = 52$) abundance peak and a small amount of Lanthanides. The latter is a Lanthanide-free model without elements of $Z > 50$. For all the models, the nucleosynthesis abundances of each Y_e are taken from Wanajo et al. (2014).

For the atomic structure calculations, we use two different codes, HULLAC (Bar-Shalom et al. 2001) and GRASP2K (Jönsson et al. 2013). The HULLAC code, which employs a parametric potential method, is used to provide atomic data for many elements while the GRASP2K code, which enables more ab-initio calculations based on the multiconfiguration Dirac-Hartree-Fock (MCDHF) method, is used to provide benchmark calculations for a few elements. Such benchmark calculations are important because systematic improvement of the accuracies is not always obtained with the HULLAC code especially when little data are available in NIST Atomic Spectra Database (ASD, Kramida et al. 2015). By using these two codes, we also study the influence of the accuracies of atomic calculations to the opacities. Tables 1 and 2 summarize the list of ions for atomic structure calculations. In the following sections, we describe our methods to calculate the atomic structures and transition probabilities.

2.1. *HULLAC*

HULLAC (Hebrew University Lawrence Livermore Atomic Code, Bar-Shalom et al. 2001) is an integrated code for calculating atomic structures and cross sections for modeling of atomic processes in plasmas and emission spectra. The latest version (9-601k) of HULLAC is used in the present work to provide atomic data for Se I-III, Ru I-III, Te I-III, Nd I-III, and Er I-III. In HULLAC, fully relativistic orbitals are used for calculations of atomic energy levels and radiative transition probabilities. The orbital functions φ_{nljm} are solutions of the single electron Dirac equation with a local central-field potential $U(r)$ which represents a nuclear field and a spherically averaged interaction with other electrons in atoms,

$$\left[c\boldsymbol{\alpha}\cdot\boldsymbol{p} + (\beta - 1)c^2 + U(r)\right]\varphi_{nljm} = \varepsilon_{nlj}\varphi_{nljm}, \quad (1)$$

Table 1
Summary of HULLAC calculations

Ion	Configurations	Number of levels	Number of lines	Subset 1[a]	Subset 2[b]
Se I	$\mathbf{4s^24p^4}$, $4s^24p^3(4d,4f,5-8l)^c$, $4s4p^5$, $4s4p^4(4d,4f)$, $4s^24p^2(4d^2,4d4f,4f^2)$, $4s4p^3(4d^2,4d4f,4f^2)$	3076	973,168	2,395	654
Se II	$\mathbf{4s^24p^3}$, $4s^24p^2(4d,4f,5-8l)^c$, $4s4p^4$, $4s4p^3(4d,4f)$, $4s^24p(4d^2,4d4f,4f^2)$, $4s4p^2(4d^2,4d4f,4f^2)$	2181	511,911	1,978	584
Se III	$\mathbf{4s^24p^2}$, $4s^24p(4d,4f,5-8l)^c$, $4s4p^3$, $4s4p^2(4d,4f)$, $4s^2(4d^2,4d4f,4f^2)$, $4s4p(4d^2,4d4f,4f^2)$	922	92,132	2,286	882
Ru I	$\mathbf{4d^75s}$, $\mathbf{4d^65s^6}$, $\mathbf{4d^8}$, $4d^7(5p,5d,6s,6p)$, $4d^65s(5p,5d,6s)$	1,545	250,476	49,181	20,350
Ru II	$\mathbf{4d^7}$, $4d^6(5s-5d,6s,6p)$	818	76,592	27,976	14,073
Ru III	$\mathbf{4d^6}$, $4d^5(5s-5d,6s)$	728	49,066	30,628	17,451
Te I	$\mathbf{5s^25p^4}$, $\mathbf{5s^25p^3}(\mathbf{4f,5d,5f,6s-6f,7s-7d,8s})$, $5s5p^5$	329	14,482	410	348
Te II	$\mathbf{5s^25p^3}$, $\mathbf{5s^25p^2}(\mathbf{4f,5d,5f,6s-6f,7s-7d,8s})$, $5s5p^4$	253	9,167	705	569
Te III	$\mathbf{5s^25p^2}$, $\mathbf{5s^25p(5d,6s-6d,7s)}$, $5s5p^3$	57	419	249	227
Nd I	$\mathbf{4f^46s^2}$, $\mathbf{4f^46s(5d,6p,7s)}$, $\mathbf{4f^45d^2}$, $\mathbf{4f^45d6p}$, $4f^35d6s^2$, $4f^35d^2(6s,6p)$, $4f^35d6s6p$	31,358	70,366,259	12,365,070	2,804,079
Nd II	$\mathbf{4f^46s}$, $\mathbf{4f^45d}$, $4f^46p$, $4f^36s(5d,6p)$, $4f^35d^2$, $4f^35d6p$	6,888	3,951,882	3,682,300	1,287,145
Nd III	$\mathbf{4f^4}$, $4f^3(5d,6s,6p)$, $4f^25d^2$, $4f^25d(6s,6p)$, $4f^26s6p$	2252	458,161	303,021	136,248
Er I	$\mathbf{4f^{12}6s^2}$, $\mathbf{4f^{12}6s(5d,6p,6d,7s,8s)}$, $4f^{11}6s^2(5d,6p)$, $4f^{11}5d^26s$, $4f^{11}5d6s(6p,7s)$	10,535	9,247,777	443,566	129,713
Er II	$\mathbf{4f^{12}6s}$, $4f^{12}(5d,6p)$, $4f^{11}6s^2$, $4f^{11}6s(5d,6p)$, $4f^{11}5d^2$, $4f^{11}5d6p$	5,333	2,432,665	1,713,258	489,383
Er III	$\mathbf{4f^{12}}$, $4f^{11}(5d,6s,6p)$	723	42,671	41,843	16,787

Note. — Configurations taken into account for optimization of central-field potentials are indicated by bold letters (see text).
[a] Number of lines whose lower level energy is $E_1 < 5$, 10, 15 eV for neutral atom and singly and doubly ionized ions, respectively.
[b] Number of lines with $\log(gf_l) \geq -3.0$ in Subset 1.
[c] $(5-8l)$ stands for single orbitals in all nl shells with $n = 5-8$ and$l = 0$ - $n-1$.

where $\boldsymbol{\alpha}$ and β are the 4×4 Dirac matrices, c the speed of light in atomic units, and ε_{nlj} an orbital energy associated with each principal quantum number n, azimuthal quantum number l, and angular quantum numbers j and m. N-electron configuration state functions (CSFs) are constructed by coupled anti-symmetrized products of the orbital functions using Racah algebra. The jj-coupling scheme is used in HULLAC.

The total Hamiltonian, which consists of the N-electron Dirac kinetic energy, the nuclear field potential, the inter-electronic interaction potential including the magnetic and retardation effects (the Breit interaction), and quantum electrodynamic (QED) energy corrections, is diagonalized with multi-CSFs (relativistic configuration interaction: RCI). Atomic energy levels are obtained from eigenvalues of the total Hamiltonian. Atomic wave functions of the energy levels are expressed as linear combinations of CSFs. Electric-dipole transition probabilities between two energy levels are obtained from the transition moments of the wave functions in length (Babushkin) gauge. In Table 1, the configuration set used in the diagonalization as well as the number of energy levels and transitions of each ion are summarized. The ground state configuration is indicated at the top. It is noted that the configuration set in the present calculations should be read as minimal. Extended sets of configurations are used for Se to get improved energy levels.

The optimal central-field potential is obtained such that energy levels of the ground state and a few excited states agree with those in the ASD. The electron charge distribution function of q electrons in an nl shell is expressed by the density of the Slater-type orbital as,

$$\rho(r) = -4\pi r^2 qA\left[r^{l+1}\exp\left(-\alpha r/2\right)\right]^2, \qquad (2)$$

where A is a normalization factor and α values represent average radii of the Slater-type orbital. The central-field potential for this electron charge distribution and the nuclear charge distribution $Z\delta(r)$ seen by an external electron is obtained from the Poisson equation with the boundary condition, $U(r)|_{r\to\infty} = (Z-q)/r$. Occupancy of each Slater-type orbital is naively chosen as the ground state configuration of the next higher charge state. The ground state configuration for each ion is as given in the ASD. Alternative occupancies will give different electron charge density distributions which result in different central-field potentials. In some cases, such alternative occupancies are used to improve results. For Ru I, an alternative occupancy [Kr] $4d^55s^2$ gives deeper and quasi-degenerate $4d$ and $5s$ orbital energies resulting in a better agreement with the energy levels of the ASD. Similarly, alternative occupancies [Xe] $4f^36s$ and [Cd] $5p^54f^{12}$ are used for Nd II and Er III, respectively, in the present calculations.

The α values which minimize first-order configuration average energies of the ground state and low-lying excited states are chosen. Such α values depend on excited state configurations added in the first-order energies to be minimized. We choose the excited state configurations by single and double substitutions of valence and

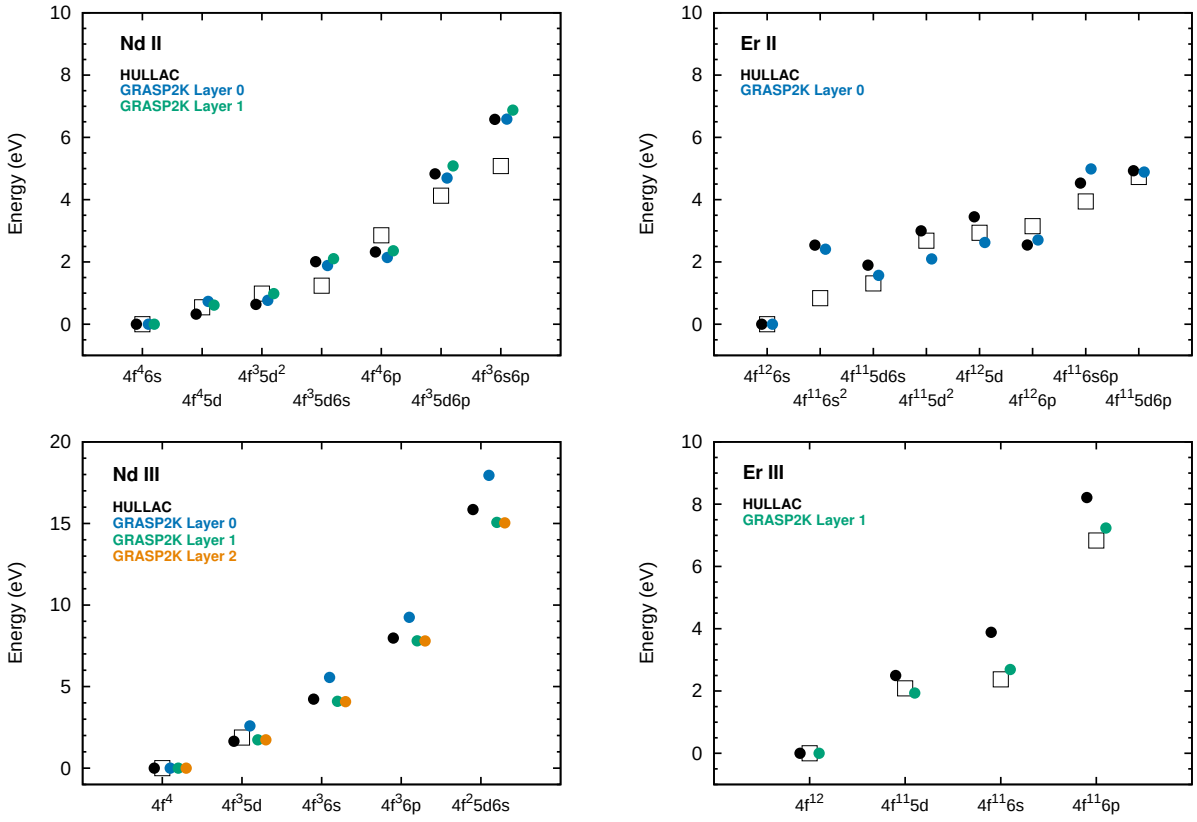

Figure 2. The excitation energy of the lowest energy levels for each electron configuration. Black circles show HULLAC calculations while blue, green, and orange circles show GRASP2K calculations with different strategies. The data from the ASD (Kramida et al. 2015) are shown in open squares for comparison.

sub-valence orbitals from the ground state configuration. The ground state for each ion as well as the excited state configurations taken into account for the energy minimization are indicated by bold letters in Table 1. Getting correct energy levels by this semi-empirical optimization takes a less computational time with limited computational resources, although systematic improvement of the results without a benchmark is not always possible. Results of a few lowest excited energy levels deviate from those of the ASD about 10% at most for Se and Te. However, we cannot obtain such close agreements for Ru reflecting complexity of the atomic structures with open d shells. Results of the energies for Nd II-III and Er II-III are shown in Figure 2 and discussed in the following section.

2.2. *GRASP2K*

GRASP2K (Jönsson et al. 2013) is used to provide atomic data for Ba II-III, Nd II-III, and Er II-III. GRASP2K is based on the MCDHF and RCI methods taking into account Breit and QED corrections (Grant 2007; Froese Fischer et al. 2016). Based on the Dirac-Coulomb Hamiltonian

$$H_{DC} = \sum_{i=1}^{N} \left(c\boldsymbol{\alpha}_i \cdot \boldsymbol{p}_i + (\beta_i - 1)c^2 + V_i^N \right) + \sum_{i>j}^{N} \frac{1}{r_{ij}}, \quad (3)$$

where V^N is the monopole part of the electron-nucleus Coulomb interaction. The atomic state functions (ASFs) are obtained as linear combinations of symmetry adapted CSFs. The CSFs are built from products of one-electron Dirac orbitals. Based on a weighted energy average of several states, the so called extended optimal level (EOL) scheme (Dyall et al. 1989), both the radial parts of the Dirac orbitals and the expansion coefficients are optimized self-consistently in the relativistic self-consistent field procedure. In the present calculations, ASFs are obtained as expansions over jj-coupled CSFs. To provide the LSJ labeling system the ASFs are transformed from a jj-coupled CSF basis into an LSJ-coupled CSF basis using the method provided by Gaigalas et al. (2017).

The MCDHF calculations are followed by RCI calculations, including the Breit interaction and leading QED effects. Note that, for Nd II and Er II, only MCDHF calculations are performed. Radiative transition data (transition probabilities, oscillator strengths) between two states built on different and independently optimized orbital sets are calculated by means of the biorthonormal transformation method (Olsen et al. 1995). For electric dipole and quadrupole (E1 and E2) transitions, we use the Babushkin gauge as in the HULLAC calculations.

In the Table 2, we give a summary of the MCDHF and RCI calculations for each of ion. As a starting point, MCDHF calculations are performed in the EOL scheme for the states of the ground configuration. The wave functions from these calculations are taken as the initial one to calculate even and odd states of multi-reference configurations. The set of orbitals belonging to these

Table 2
Summary of GRASP2K calculations

Ion	Inact. core	Ground conf.	multi-reference set Even	multi-reference set Odd	Active set	Number of levels Even	Number of levels Odd	N_{CSFs} Even	N_{CSFs} Odd
Ba II	[Kr]	$4d^{10}5s^25p^66s$	$4d^{10}5s^25p^6ns$ $4d^{10}5s^25p^6(n-1)d$ $4d^{10}5s^25p^6(n-1)g$ $n=6-20$	$4d^{10}5s^25p^6np$ $4d^{10}5s^25p^6(n-2)f$	$\{ns, np, (n-1)d,$ $(n-2)f, (n-1)g\}$	75	60	838,672	614,880
Ba III	[Kr]	$4d^{10}5s^25p^6$	$4d^{10}5s^25p^6$ [a] $4d^{10}5s^25p^5np$ $4d^{10}5s^25p^5(n-2)f$ $4d^{10}5s^25p^5nh$ [a] $n=6-23$	$4d^{10}5s^25p^5ns$ $4d^{10}5s^25p^5(n-1)d$ $4d^{10}5s^25p^5(n-1)g$	$\{ns, np, (n-1)d,$ $(n-2)f, (n-1)g$ $nh^a\}$	409	504	70,067	71,388
Nd II	[Xe]	$4f^46s$	$4f^46s$, $4f^45d$ $4f^35d6p$, $4f^36s6p$	$4f^35d^2$, $4f^46p$ $4f^35d6s$	{7s,7p,6d,5f}	3,890	2,998	24,568	23,966
Nd III	[Xe]	$4f^4$	$4f^4$, $4f^36p$ $4f^25d^2$, $4f^25d6s$ [b]	$4f^35d$, $4f^36s$	{8s,8p,7d,6g,6h}	1,020	468	173,816	114,621
Er II	[Xe]	$4f^{12}6s$	$4f^{12}6s$, $4f^{12}5d$ $4f^{11}5d6p$, $4f^{11}6s6p$	$4f^{11}5d6s$, $4f^{11}5d^2$ $4f^{11}6s^2$, $4f^{12}6p$	{7s,7p,6d,5f}	2,836	2,497	22,460	21,731
Er III	[Xe]	$4f^{12}$	$4f^{12}$, $4f^{11}6p$	$4f^{11}5d$, $4f^{11}6s$	{7s,7p,6d,5f}	255	468	503,824	842,643

Note. — Summary of the MCDHF and RCI calculations indicating inactive core, multi-reference set, active set, number of calculated levels and number of configuration state functions (N_{CSFs}) in the final list for each of parity.
[a] Ground state and states of the configuration $4d^{10}5s^25p^5nh$ as the nh orbital were excluded from the computations for $n = 7 - 23$.
[b] To match with the configurations used by Kasen et al. (2013), the $4f^25d6p$ configuration is not included in the GRASP2K calculations while it is included in the HULLAC calculations. As a result, the HULLAC results have more energy levels (2252) compared with those of GRASP2K (1488). This difference does not have a big impact on the opacities as the energy levels from the configuration is rather high.

multi-reference configurations are referred to Layer 0. After that the even and odd states are calculated separately. Unless stated otherwise, in the present calculations the inactive core for each of ions is mentioned in Table 2. The CSF expansions for states of each parity are obtained by allowing single and double substitutions from the multi-reference configurations up to active orbital sets (see Table 2). The configuration space was increased step by step with increasing layer number. The orbitals of previous layers are held fixed and only the orbitals of the new layer are allowed to vary.

2.3. *Results*

Figure 2 shows the derived lowest energy for each electron configuration of Nd II, Nd III, Er II, and Er III ions. For Nd II, both HULLAC and GRASP2K calculations show reasonable agreement with the data in the ASD (open squares). Our calculations provides the correct orders of energy levels, and the deviation from the energy in the ASD is about $\lesssim 30\%$ except for the $4f^36s6p$ configuration. Overall agreement is slightly better than that obtained by Kasen et al. (2013) with Autostructure code (Badnell 2011). For Nd III, the energy of the excited level is available only for $4f^35d$ and our calculations give an excellent agreement except for the Layer 0 calculation of GRASP2K (blue points).

For the case of Er, the agreement with the ASD is not as good as in the Nd ions, which reflects the complexity of the Er ions. For Er II, both HULLAC and GRASP2K calculations do not give the correct order of energy: the derived energy of $4f^{11}6s^2$ is too high. On the other hand, for Er III, the orders of energy are reproduced well although the number of available data in the ASD is small. For the case of Er III, GRASP2K results give a better agreement than HULLAC. In the next section, we discuss the influence of these results to the opacities.

3. OPACITY

We calculate the bound-bound opacities by using the energy levels and the transition probabilities obtained from our atomic structure calculations. For bound-bound opacities, we use the formalism of expansion opacity Karp et al. (1977); Eastman & Pinto (1993); Kasen et al. (2006);

$$\alpha^{\rm bb}_{\rm exp}(\lambda) = \frac{1}{ct}\sum_l \frac{\lambda_l}{\Delta\lambda}(1-e^{-\tau_l}), \quad (4)$$

which are also adopted by previous studies of kilonova simulations (Kasen et al. 2013; Barnes & Kasen 2013; Tanaka & Hotokezaka 2013; Tanaka et al. 2014). Here τ_l is the Sobolev optical depth for a transition, and it can be written as

$$\tau_l = \frac{\pi e^2}{m_e c} f_l n_l t \lambda_l \quad (5)$$

for homologously expanding ejecta. Here, λ_l and f_l are the wavelength and the oscillator strength of the transition, respectively, and n_l is the number density of the lower level of the transition. The summation in the expansion opacity is taken for all the transition within a wavelength bin ($\Delta\lambda$). The number density of each ion is calculated under the assumption of local thermodynamic equilibrium, and the population of the excited levels is calculated by assuming the Boltzmann distribution.

We confirm that there is an overall trend that the bound-bound opacities of open f-shell (Lanthanide) elements are higher than those of open s-shell, p-shell, and d-shell elements over the wide wavelength range. The opacities of open d-shell elements (Fe and Ru) concentrates on the ultraviolet and optical wavelengths, and those of open s-shell (Ba) and p-shell (Se and Te) elements also have a similar trend with even lower opacities.

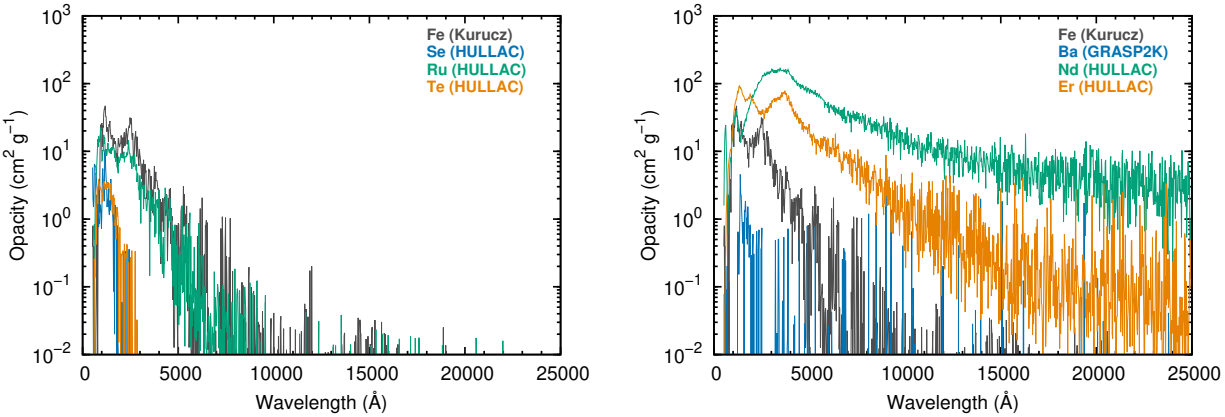

Figure 3. Line expansion opacities of Se, Ru, Te (left), Ba, Nd, and Er (right). The calculations assume $\rho = 1 \times 10^{-13}$ g cm^{-3}, $T = 5,000$ K, and $t = 1$ day after the merger. The results are compared with the line expansion opacities of Fe calculated with Kurucz's line list.

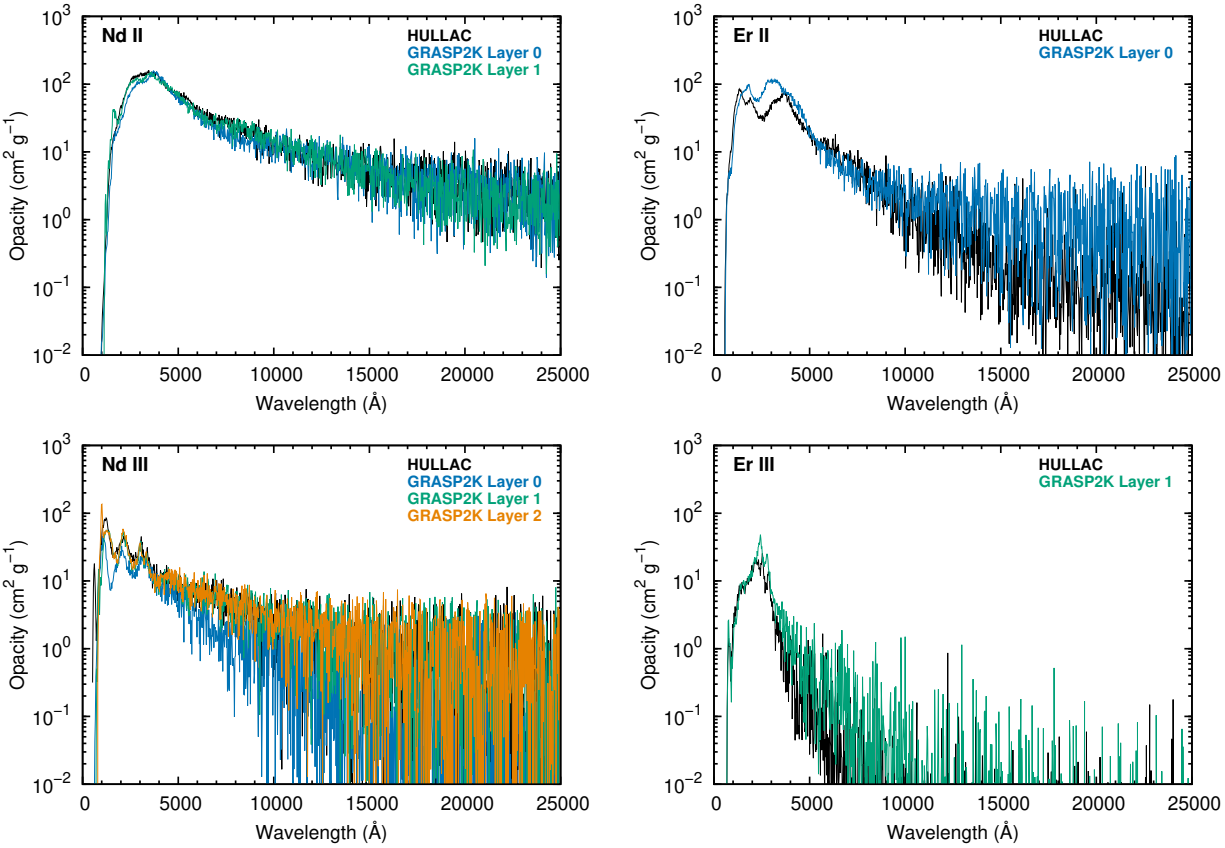

Figure 4. Comparison of line expansion opacities between HULLAC and GRASP2K calculations. For singly ionized ions (Nd II and Er II), the calculations assume $\rho = 1 \times 10^{-13}$ g cm^{-3}, $T = 5,000$ K, and $t = 1$ day after the merger. For doubly ionized ions (Nd III and Er III), the calculations assume the same density at the same epoch but $T = 10,000$ K.

Figure 3 shows the opacity of each element calculated with $\rho = 1 \times 10^{-13}$ g cm^{-3}, $T = 5,000$ K, and $t = 1$ day after the merger. For comparison, Fe opacities with Kurucz's line list (Kurucz & Bell 1995) are also shown. The opacities of Nd and Er (open f-shell) are much higher than that of Fe (open d-shell). The opacity of Ru (open d-shell) is similar to that of Fe, which demonstrates the similarity in the opacity for the elements with the same open shell. The same is true for open p-shell; the opacities of Se and Te are found to be similar.

The opacities from the two atomic codes agree reasonably well. Figure 4 shows the line expansion opacities of Nd II, Nd III, Er II, and Er III. As expected from the good agreement in the energy levels (Figure 2), the opacities from HULLAC and GRASP2K are almost indistinguishable for Nd II and Nd III. It is noted that, only the Layer 0 calculations with GRASP2K gives Nd III opacities lower than more realistic (Layer 1 and Layer 2) cal-

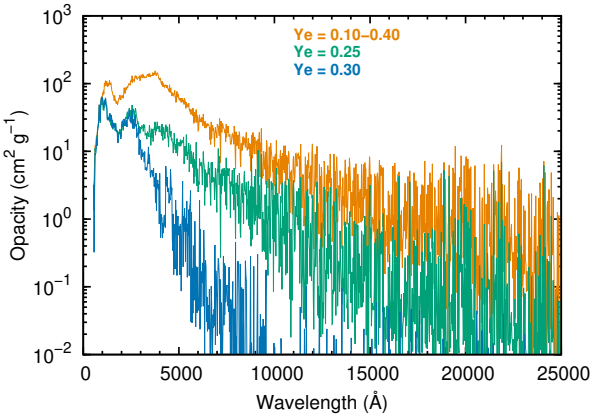

Figure 5. Line expansion opacities for mixture of elements in the ejecta of NS mergers (see Figure 1). The orange line represents the opacity in the dynamical ejecta, which is calculated with the abundance pattern of $Y_e = 0.10 - 0.40$. The blue and green lines represent the opacities in the high-Y_e post-merger ejecta, which are calculated with the abundance patterns of $Y_e = 0.25$ and 0.30, respectively. All the calculations assume $\rho = 1 \times 10^{-13}$ g cm^{-3}, $T = 5,000$ K, and $t = 1$ day after the merger.

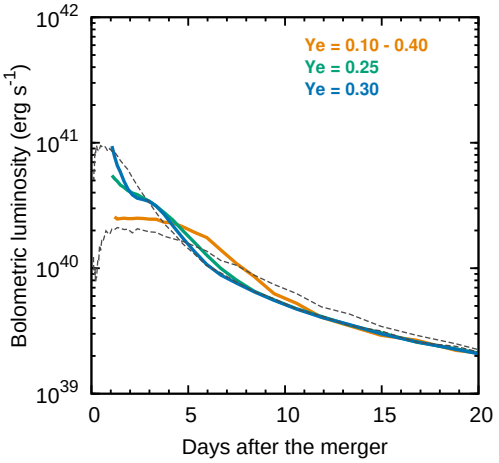

Figure 6. Bolometric light curves of simple NS merger models with $M_{ej} = 0.01 M_\odot$ and $v_{ch} = 0.1c$. The solid curves show the results with the wavelength-dependent radiative transfer for different abundance ratios according to Figure 1: $Y_e = 0.10 - 0.40$ (orange), $Y_e = 0.25$ (green), and $Y_e = 0.30$ (blue). The dashed lines shows the results with the gray radiative transfer with the gray opacity of 1.0 and 10.0 cm^2 g^{-1} from top to bottom. For all the models, the analytic heating rates are used and constant thermalization efficiency ($\epsilon = 0.25$) is assumed.

culations. This is because the Layer 0 calculations give higher energy levels (Figure 2), which reduces the contribution of bound-bound transitions involving excited levels for a given temperature.

For the Er ions, we find that two atomic codes give larger discrepancies in the energy levels compared with the cases of Nd ions. As in the case of Nd III, opacities of Er II and Er III from HULLAC calculations are slightly smaller that those from GRASP2K calculations because HULLAC calculations give slightly higher energy levels for the excited energy levels. However, the difference in the opacity is only up to a factor of about 2. Therefore, we conclude that a relatively simplified calculations with the HULLAC code gives opacities with sufficient accuracies for astronomical applications.

Finally we calculate the opacities for mixture of elements. We use the HULLAC results which cover more elements and ionization states. Because we have atomic structure calculations for a small number of elements, we assume the same bound-bound transition properties for the elements with the same open shell (see Figure 1). For open f-shell elements, the former and latter halfs are replaced with Nd and Er, respectively. For the heavy elements with $Z > 71$, we repeat to use the data of Ru, Te, Nd, and Er. For the elements with $Z < 32$, we use Kurucz's line list (Kurucz & Bell 1995). We neglect the contribution of open s-shell elements because the total fraction of these elements are small in the ejecta (Figure 1) and the opacities are subdominant (Figure 3).

As a result of high opacity of Lanthanide elements, the opacities for the mixture of elements depends significantly on Y_e. Figure 5 shows the line expansion opacity for the element mixture in the dynamical ejecta ($Y_e = 0.10 - 0.40$) and high-Y_e ejecta ($Y_e = 0.25$ and 0.30). If the ejecta is completely Lanthanide free as in the case of $Y_e = 0.30$, the line expansion opacity is smaller than that in the Lanthanide-rich ejecta by a factor of > 10 near the middle of optical range (~ 5000 Å). However, small inclusion of Lanthanide elements dramatically enhances the opacities as shown in the case of $Y_e = 0.25$. This demonstrates the importance of accurate Y_e determination in the merger simulations for the accurate prediction of kilonova signals.

4. RADIATIVE TRANSFER SIMULATIONS

We perform radiative transfer simulations by using our new atomic data. We use three-dimensional, time-dependent, wavelength-dependent Monte Carlo radiative transfer code (Tanaka & Hotokezaka 2013). The code takes into account electron scattering and bound-bound, bound-free, and free-free transitions as sources of opacity. In the previous version of the code (Tanaka & Hotokezaka 2013; Tanaka et al. 2014; Tanaka 2016), we use the VALD database (Piskunov et al. 1995; Ryabchikova et al. 1997; Kupka et al. 1999, 2000) for the bound-bound transitions, while in this paper we use our atomic data presented in Section 2 and treat element mixture by using representative elements as described in Section 3. To save the memory space in the computation, we use a subset of the line list including the transitions whose lower level energy is $E_1 < 5$, 10, 15 eV for neutral atom and singly and doubly ionized ions, respectively (Subset 1 in Table 1) and whose oscillator strengths are $\log(gf_l) \geq -3.0$ (Subset 2 in Table 1). We confirm that the use of this subset does not significantly affect the calculated light curves and spectra.

4.1. *Simple models*

To study the effect of the element abundances (or Y_e) on the light curves, we calculate the light curves for the three different abundance patterns displayed in Figure 1. For ease to extract the effect of opacities on the element abundances, we employ a simple model of NS merger ejecta, of which parameters are set to be the same for three cases. The ejecta mass is taken to be $M_{ej} = 0.01 M_\odot$. The density structure of the ejecta is assumed to be spherical with a power-law radial profile of $\rho \propto r^{-3}$ from $v = 0.05c$ to $0.2c$ (Metzger et al. 2010;

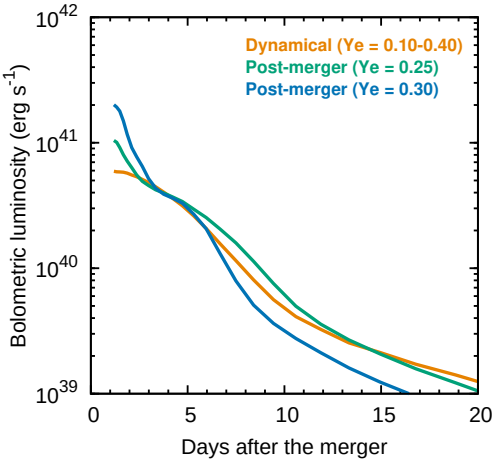

Figure 7. Bolometric light curves of dynamical and post-merger ejecta models. The orange line shows the NS merger model APR4-1215 (Hotokezaka et al. 2013a) with $M_{\rm ej} = 0.01 M_\odot$ and the element abundances of $Y_{\rm e} = 0.10 - 0.40$ in Figure 1. Blue and green lines show the post-merger ejecta models (power-law density profile with $M_{\rm ej} = 0.01 M_\odot$ and $v_{\rm ch} = 0.05c$) with the element abundances of $Y_{\rm e} = 0.30$ and 0.25, respectively. For all the models, the heating rates from nucleosynthesis calculations (Wanajo et al. 2014) are used and the thermalization efficiencies (Barnes et al. 2016) are taken into account.

Tanaka & Hotokezaka 2013; Metzger 2017). This model has a characteristic velocity of $v_{\rm ch} = \sqrt{2E_{\rm K}/M_{\rm ej}} = 0.1c$, where $E_{\rm K}$ is the kinetic energy of the ejecta.

For the heating rate of radioactive decays, we adopt $2 \times 10^{10} t_{\rm d}^{-1.3}$ erg s^{-1} g^{-1} ($t_{\rm d}$ is the time after the merger in days), which gives a reasonable agreement with nucleosynthesis calculations for a wide range of $Y_{\rm e}$ (Wanajo et al. 2014). We assume that a thermalization factor (ϵ), that is, a fraction of the decay energy deposited to the ejecta, is time-independent, and adopt $\epsilon = 0.25$, which is a typical value at a few days after the merger (Barnes et al. 2016; Rosswog et al. 2017).

Figure 6 shows the bolometric light curves of the simple models. Overall properties of the bolometric light curves can be understood by the dependence on the opacities; the characteristic timescale becomes shorter and the luminosity becomes higher for smaller opacities. As a result, the models with $Y_{\rm e} = 0.25$ and 0.30 has higher bolometric luminosities at the first few days.

For comparison, we also show the results with gray transfer simulations with $\kappa = 1.0$ and 10 cm^2 g^{-1}. It should be noted, however, that the gray opacities give a reasonable approximation only for the bolometric luminosity. Properties of multi-color light curves cannot be well described by the gray opacities as expected from the strong wavelength dependence of the opacities (Figure 5).

4.2. *Realistic Models*

We perform radiative transfer simulations for more realistic models of dynamical and high-$Y_{\rm e}$ post-merger ejecta. For the dynamical ejecta model, we use the density structure from the results of numerical relativity simulations by Hotokezaka et al. (2013a). As a representative case, we use the APR4-1215 model, which is the merger of two NSs with the gravitational masses of $1.2 M_\odot$ and $1.5 M_\odot$. The ejecta mass is $M_{\rm ej} = 0.01 M_\odot$ and the characteristic velocity is $v_{\rm ch} = 0.24c$.

The dynamical ejecta have a wide range of $Y_{\rm e}$, which composes of the low-$Y_{\rm e}$ tidally disrupted component and the high-$Y_{\rm e}$ component by shock heating and/or neutrino absorption (Wanajo et al. 2014; Sekiguchi et al. 2015; Goriely et al. 2015; Sekiguchi et al. 2016; Radice et al. 2016; Foucart et al. 2016; Lehner et al. 2016). Therefore, we approximate the calculated abundance patterns in Wanajo et al. (2014) by a flat $Y_{\rm e}$ distribution from 0.10 to 0.40 as described in Section 2 (orange line in Figure 1). We assume spatially homogeneous element distribution for simplicity although merger simulations suggest that the polar regions consist mainly of high $Y_{\rm e}$ material (e.g., Sekiguchi et al. 2016).

For models of post-merger ejecta, which originate from several possible mechanisms such as viscosity, neutrino heating, and nuclear recombination, we keep using a simple spherical model with a power-law profile as in Section 4.1, instead of using results of numerical simulations. We set $M_{\rm ej} = 0.01 M_\odot$ as a representative case. Because the typical velocity of the post-merger ejecta tends to be lower than that of the dynamical ejecta, we set the velocity range from $v = 0.02c$ to $0.1c$, which gives a characteristic velocity of $v_{\rm ch} = 0.05c$. The element abundances in the ejecta can vary depending on the detailed mechanisms of mass ejection. In this paper, to study the effect of Lanthanide-free ejecta, we assume relatively high $Y_{\rm e}$, that is, $Y_{\rm e} = 0.25$ and 0.30 as shown in Figure 1. The spatial distribution of the elements are assumed to be homogeneous as in the dynamical ejecta.

For both dynamical and post-merger ejecta models, we use the heating rates from nucleosynthesis calculations for relevant $Y_{\rm e}$ in Wanajo et al. (2014). The radioactive decay and subsequent energy deposition from β-decay, α-decay, and fission are taken into account. For the β-decay, 45% and 20% of energy are assumed to be carried out by γ-rays and β particles, respectively. Then, thermalization efficiencies of γ-rays, α particles, β particles, and fission fragments are independently evaluated by using analytic descriptions in Barnes et al. (2016).

Figure 7 shows the bolometric light curves for all the models. Overall properties of the bolometric light curves are similar to the simple models in Section 4.1. The luminosity of each model at a few days after the merger is, however, higher than that of the simple model because the thermalization factor is higher than 0.25 at the early time. At $\gtrsim 5$ days after the merger, the luminosities decline faster than those in the simple models due to decreasing thermalization efficiency. This trend is most notable for the case of $Y_{\rm e} = 0.3$ because of the smallest amounts of the second peak elements with $Z \sim 50$ (see Figure 1) that have dominant contributions to the radioactive heating (Metzger et al. 2010; Wanajo et al. 2014). At late times (> 14 days) when the heating from fission becomes important (Wanajo et al. 2014; Hotokezaka et al. 2016), the dynamical ejecta model (of $Y_{\rm e} = 0.1 - 0.4$) that contains the transuranic elements gives the highest luminosity.

Figures 8 and 9 show the multi-color light curves and spectra for three models, respectively. The spectra of the dynamical ejecta model (APR4-1215) are very red, which peaks in near infrared at $t = 1 - 20$ days. On the other hand, the post-merger ejecta model with $Y_{\rm e} = 0.3$

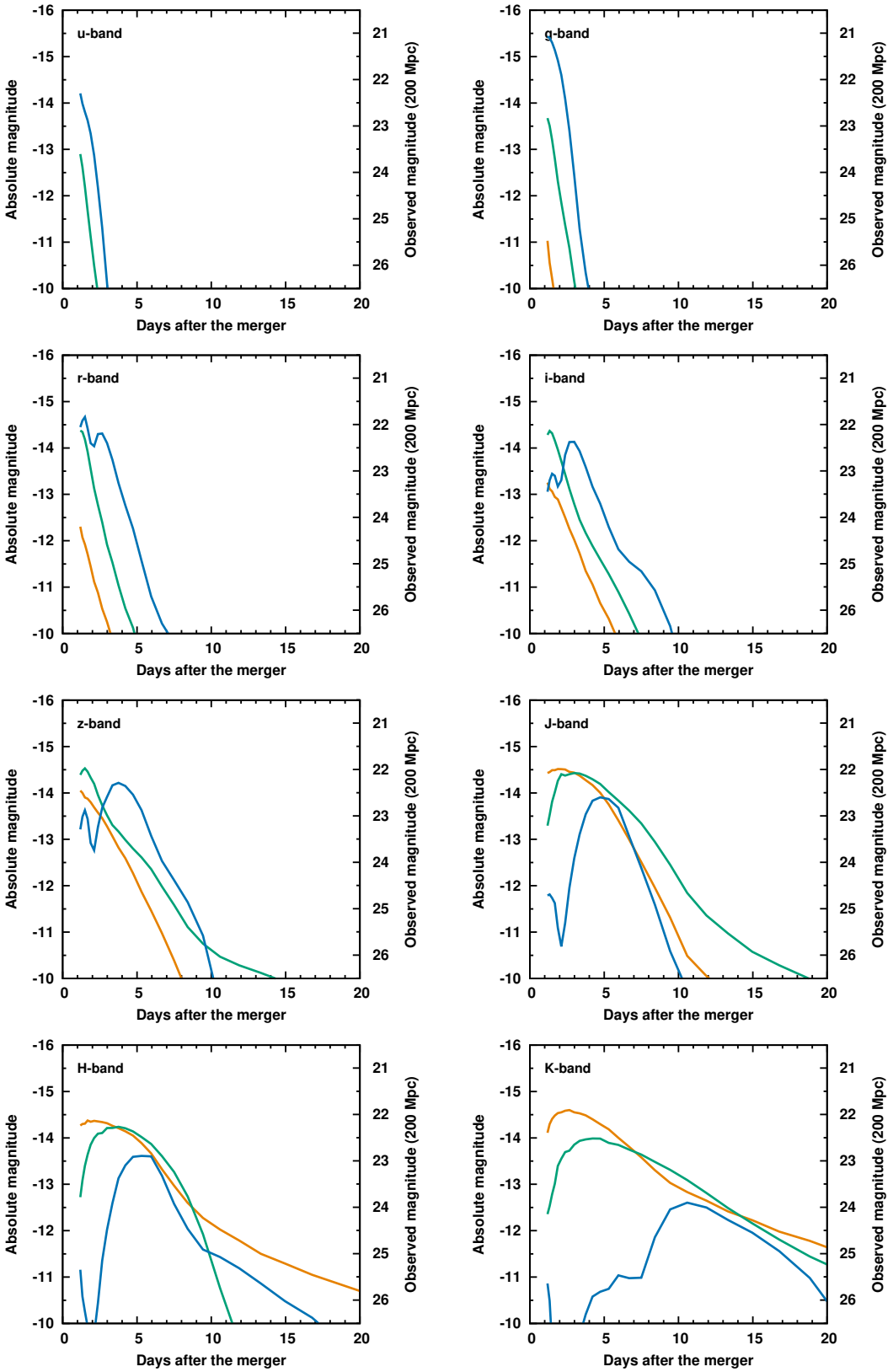

Figure 8. Multi-color ($ugrizJHK$-band) light curves for the dynamical ejecta model APR4-1215 with $Y_{\rm e} = 0.10 - 0.40$ (orange) and the post-merger ejecta models with $Y_{\rm e} = 0.30$ (blue) and 0.25 (green). The vertical axis on the left shows the absolute magnitude while that on the right the observed magnitude at 200 Mpc. All the magnitudes are given in AB magnitudes.

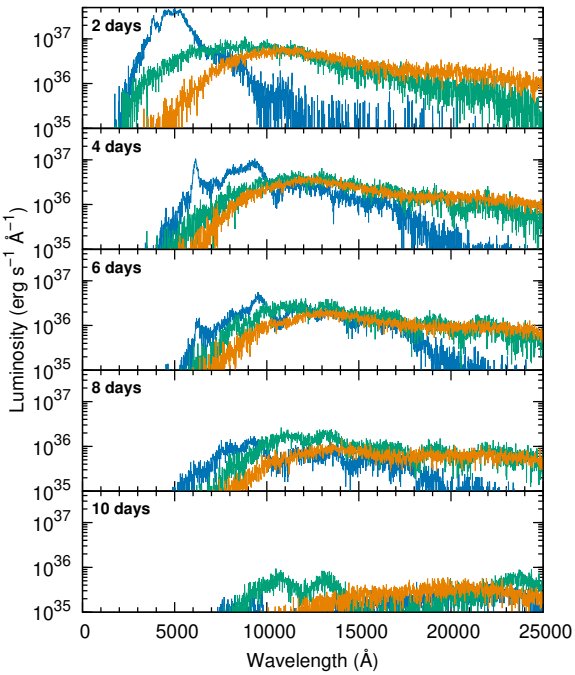

Figure 9. Spectra of dynamical and post-merger ejecta models at $t = 2$, 4, 6, 8, and 10 days after the merger. The orange line shows the NS merger model APR4-1215 (Hotokezaka et al. 2013a) with $M_{\rm ej} = 0.01 M_\odot$ and the element abundances of $Y_{\rm e} = 0.10 - 0.40$ in Figure 1. Blue and green lines show the post-merger ejecta models (power-law density profile with $M_{\rm ej} = 0.01 M_\odot$ and $v_{\rm ch} = 0.05c$) with the element abundances of $Y_{\rm e} = 0.30$ and 0.25, respectively.

has a peak in optical at $t \lesssim 5$ days. As a result, the post-merger ejecta model with $Y_{\rm e} = 0.3$ is much brighter than the dynamical ejecta model in optical, especially in u, g, and r bands.

The properties of the light curves of the post-merger ejecta model with $Y_{\rm e} = 0.25$ are in between the other two models, as expected from the intermediate opacities. Therefore, this model has hybrid properties; the optical brightness is higher than that of dynamical ejecta model and the near-infrared brightness is not as faint as that of the post-merger ejecta with $Y_{\rm e} = 0.3$ (Figure 9).

Our results confirm the presence of "blue kilonova" that was previously suggested based on the use of iron opacity for the light r-process elements (Metzger & Fernández 2014; Kasen et al. 2015). For 0.01 $M_\odot$ of Lanthanide-free ($Y_{\rm e} = 0.3$) ejecta, the optical brightness reaches the absolute magnitude of $M = -14$ mag in g and r bands within a few days after the merger. This corresponds to 21.0 mag and 22.5 mag at 100 Mpc and 200 Mpc, respectively. Thanks to the relatively blue color, this emission is detectable with 1m-class and 2m-class telescopes, respectively.

It should be noted that the observability of blue kilonova from Lanthanide-free post-merger ejecta depends on the properties of preceding dynamical ejecta as discussed in Kasen et al. (2015). If Lanthanide-rich dynamical ejecta are present in all the direction, the blue kilonova emission is likely to be absorbed. However, recent relativistic simulations with neutrino interaction show that dynamical ejecta can have relatively high $Y_{\rm e}$ near the polar regions (see, e.g., Sekiguchi et al. 2015; Radice et al. 2016; Foucart et al. 2016). In such case, the blue emission from the post-merger ejecta can be observable from the polar direction without being absorbed. To test this hypothesis, it is necessary to consistently model the dynamical and post-merger ejecta. It is also noted that our simulations cannot predict the emission within ~ 1 day after the merger due to lack of the atomic data of more ionized elements. Emission at such early times can peak at optical or even ultraviolet wavelengths (Metzger et al. 2015; Gottlieb et al. 2017), and therefore, it will also be a good target for follow-up observations especially with small telescopes.

5. SUMMARY

We have newly performed atomic structure calculations for Se ($Z = 34$), Ru ($Z = 44$), Te ($Z = 52$), Ba ($Z = 56$), Nd ($Z = 60$), and Er ($Z = 68$) to construct the atomic data for a wide range of r-process elements. By using two different atomic codes, we confirmed that the atomic structure calculations gave uncertainties in opacities by only a factor of up to about 2. We found that the opacities from the bound-bound transitions of open f-shell elements were the highest from ultraviolet to near-infrared wavelengths, while those of open s-shell, d-shell, and p-shell elements were lower and concentrated in ultraviolet and optical wavelengths.

Using our new atomic data, we performed multi-wavelength radiative transfer simulations to predict a possible variety of kilonova emission. We found that, even for the same ejecta mass, the optical brightness varied by > 2 mag depending on the distribution of elemental abundances. If the blue emission from the post-merger, Lanthanide-free ejecta with 0.01 $M_\odot$ is observable without being absorbed by preceding dynamical ejecta, the brightness will reach the absolute magnitude of $M = -14$ mag in g and r bands within a few days after the merger. This corresponds to 21.0 mag and 22.5 mag at 100 Mpc and 200 Mpc, which is detectable with 1m-class and 2m-class telescopes, respectively.

We thank Kenta Hotokezaka, Masaru Shibata, Nobuya Nishimura, Kenta Kiuchi, and Koutarou Kyutoku for providing results of simulations and fruitful discussion. MT thanks the Institute for Nuclear Theory (INT) at the University of Washington for its hospitality and the Department of Energy for partial support during the completion of this work. MT also thanks Rodrigo Fernández, Brian Metzger, Daniel Kasen, and Gabriel Martinez-Pinedo for organizing the workshop and providing the nice research environment at INT. Numerical simulations presented in this paper were carried out with Cray XC30 at Center for Computational Astrophysics, National Astronomical Observatory of Japan. Computations by GG were performed on resources at the High Performance Computing Center "HPC Sauletekis" of the Faculty of Physics at Vilnius University. This research was supported by the NINS program for cross-disciplinary science study, Inoue Science Research Award from Inoue Foundation for Science, the RIKEN iTHES project, a post-K computer project (Priority issue No. 9) of MEXT, and the Grant-in-Aid for Scientific Research from JSPS (15H00782, 15H02075, 15K05077, 16H02183,

16H06341, 16K17706, 17K05391, 26400237) and MEXT (17H06357, 17H06363).

REFERENCES

Abbott, B. P., et al. 2016a, Physical Review Letters, 116, 241103
—. 2016b, ApJ, 826, L13
—. 2016c, Physical Review Letters, 116, 061102
—. 2017, Physical Review Letters, 118, 221101
Abbott, B. P., LIGO Scientific Collaboration, & Virgo Collaboration. 2016d, Living Reviews in Relativity, 19
Badnell, N. R. 2011, Computer Physics Communications, 182, 1528
Bar-Shalom, A., Klapisch, M., & Oreg, J. 2001, J. Quant. Spec. Radiat. Transf., 71, 169
Barnes, J., & Kasen, D. 2013, ApJ, 775, 18
Barnes, J., Kasen, D., Wu, M.-R., & Martínez-Pinedo, G. 2016, ApJ, 829, 110
Berger, E., Fong, W., & Chornock, R. 2013, ApJ, 774, L23
Ciolfi, R., Kastaun, W., Giacomazzo, B., Endrizzi, A., Siegel, D. M., & Perna, R. 2017, Phys. Rev. D, 95, 063016
Cowperthwaite, P. S., et al. 2016, ApJ, 826, L29
Dessart, L., Ott, C. D., Burrows, A., Rosswog, S., & Livne, E. 2009, ApJ, 690, 1681
Dyall, K. G., Grant, I. P., Johnson, C. T., Parpia, F. A., & Plummer, E. P. 1989, Computer Physics Communications, 55, 425
Eastman, R. G., & Pinto, P. A. 1993, ApJ, 412, 731
Fernández, R., Kasen, D., Metzger, B. D., & Quataert, E. 2015a, MNRAS, 446, 750
Fernández, R., & Metzger, B. D. 2013, MNRAS, 435, 502
—. 2016, Annual Review of Nuclear and Particle Science, 66, 23
Fernández, R., Quataert, E., Schwab, J., Kasen, D., & Rosswog, S. 2015b, MNRAS, 449, 390
Fontes, C. J., Fryer, C. L., Hungerford, A. L., Wollaeger, R. T., Rosswog, S., & Berger, E. 2017, arXiv:1702.02990
Foucart, F., O'Connor, E., Roberts, L., Kidder, L. E., Pfeiffer, H. P., & Scheel, M. A. 2016, Phys. Rev. D, 94, 123016
Froese Fischer, C., Godefroid, M., Brage, T., Jönsson, P., & Gaigalas, G. 2016, Journal of Physics B Atomic Molecular Physics, 49, 182004
Fujibayashi, S., Sekiguchi, Y., Kiuchi, K., & Shibata, M. 2017, arXiv:1703.10191
Gaigalas, G., Fischer, C., Rynkun, P., & Jönsson, P. 2017, Atoms, 5, 6
Giacomazzo, B., Zrake, J., Duffell, P. C., MacFadyen, A. I., & Perna, R. 2015, ApJ, 809, 39
Goriely, S., Bauswein, A., Just, O., Pllumbi, E., & Janka, H.-T. 2015, MNRAS, 452, 3894
Gottlieb, O., Nakar, E., & Piran, T. 2017, arXiv:1705.10797
Grant, I. P. 2007, Relativistic Quantum Theory of Atoms and Molecules (Springer Science+Business Media)
Hotokezaka, K., Kiuchi, K., Kyutoku, K., Okawa, H., Sekiguchi, Y., Shibata, M., & Taniguchi, K. 2013a, Phys. Rev. D, 87, 024001
Hotokezaka, K., Kyutoku, K., Tanaka, M., Kiuchi, K., Sekiguchi, Y., Shibata, M., & Wanajo, S. 2013b, ApJ, 778, L16
Hotokezaka, K., Wanajo, S., Tanaka, M., Bamba, A., Terada, Y., & Piran, T. 2016, MNRAS, 459, 35
Jin, Z.-P., et al. 2016, Nature Communications, 7, 12898
Jin, Z.-P., Li, X., Cano, Z., Covino, S., Fan, Y.-Z., & Wei, D.-M. 2015, ApJ, 811, L22
Jönsson, P., Gaigalas, G., Bieroń, J., Fischer, C. F., & Grant, I. P. 2013, Computer Physics Communications, 184, 2197
Just, O., Bauswein, A., Pulpillo, R. A., Goriely, S., & Janka, H.-T. 2015, MNRAS, 448, 541
Karp, A. H., Lasher, G., Chan, K. L., & Salpeter, E. E. 1977, ApJ, 214, 161
Kasen, D., Badnell, N. R., & Barnes, J. 2013, ApJ, 774, 25
Kasen, D., Fernández, R., & Metzger, B. D. 2015, MNRAS, 450, 1777
Kasen, D., Thomas, R. C., & Nugent, P. 2006, ApJ, 651, 366
Kasliwal, M. M., et al. 2016, ApJ, 824, L24
Kiuchi, K., Kyutoku, K., Sekiguchi, Y., Shibata, M., & Wada, T. 2014, Phys. Rev. D, 90, 041502
Kiuchi, K., Sekiguchi, Y., Kyutoku, K., Shibata, M., Taniguchi, K., & Wada, T. 2015, Phys. Rev. D, 92, 064034
Kramida, A., Yu. Ralchenko, Reader, J., & and NIST ASD Team. 2015, NIST Atomic Spectra Database (ver. 5.3) `http://physics.nist.gov/asd`. National Institute of Standards and Technology, Gaithersburg, MD.
Kulkarni, S. R. 2005, arXiv:astro-ph/0510256
Kupka, F., Piskunov, N., Ryabchikova, T. A., Stempels, H. C., & Weiss, W. W. 1999, A&AS, 138, 119
Kupka, F. G., Ryabchikova, T. A., Piskunov, N. E., Stempels, H. C., & Weiss, W. W. 2000, Baltic Astronomy, 9, 590
Kurucz, R., & Bell, B. 1995, Atomic Line Data (R.L. Kurucz and B. Bell) Kurucz CD-ROM No. 23. Cambridge, Mass.: Smithsonian Astrophysical Observatory, 1995., 23
Lehner, L., Liebling, S. L., Palenzuela, C., Caballero, O. L., O'Connor, E., Anderson, M., & Neilsen, D. 2016, Classical and Quantum Gravity, 33, 184002
Li, L.-X., & Paczyński, B. 1998, ApJ, 507, L59
Lippuner, J., Fernández, R., Roberts, L. F., Foucart, F., Kasen, D., Metzger, B. D., & Ott, C. D. 2017, arXiv:1703.06216
Martin, D., Perego, A., Arcones, A., Thielemann, F.-K., Korobkin, O., & Rosswog, S. 2015, ApJ, 813, 2
Metzger, B. D. 2017, Living Reviews in Relativity, 20, 3
Metzger, B. D., Bauswein, A., Goriely, S., & Kasen, D. 2015, MNRAS, 446, 1115
Metzger, B. D., & Berger, E. 2012, ApJ, 746, 48
Metzger, B. D., & Fernández, R. 2014, MNRAS, 441, 3444
Metzger, B. D., et al. 2010, MNRAS, 406, 2650
Morokuma, T., et al. 2016, PASJ, 68, L9
Olsen, J., Godefroid, M. R., Jönsson, P., Malmqvist, P. Å., & Fischer, C. F. 1995, Phys. Rev. E, 52, 4499
Perego, A., Rosswog, S., Cabezón, R. M., Korobkin, O., Käppeli, R., Arcones, A., & Liebendörfer, M. 2014, MNRAS, 443, 3134
Piran, T., Korobkin, O., & Rosswog, S. 2014, arXiv:1401.2166
Piskunov, N. E., Kupka, F., Ryabchikova, T. A., Weiss, W. W., & Jeffery, C. S. 1995, A&AS, 112, 525
Price, D. J., & Rosswog, S. 2006, Science, 312, 719
Radice, D., Galeazzi, F., Lippuner, J., Roberts, L. F., Ott, C. D., & Rezzolla, L. 2016, MNRAS, 460, 3255
Rosswog, S. 2015, International Journal of Modern Physics D, 24, 1530012
Rosswog, S., Feindt, U., Korobkin, O., Wu, M.-R., Sollerman, J., Goobar, A., & Martinez-Pinedo, G. 2017, Classical and Quantum Gravity, 34, 104001
Ryabchikova, T. A., Piskunov, N. E., Kupka, F., & Weiss, W. W. 1997, Baltic Astronomy, 6, 244
Sekiguchi, Y., Kiuchi, K., Kyutoku, K., & Shibata, M. 2015, Phys. Rev. D, 91, 064059
Sekiguchi, Y., Kiuchi, K., Kyutoku, K., Shibata, M., & Taniguchi, K. 2016, Phys. Rev. D, 93, 124046
Shibata, M., Kiuchi, K., & Sekiguchi, Y. 2017, Phys. Rev. D, 95, 083005
Siegel, D. M., & Metzger, B. D. 2017, arXiv:1705.05473
Simmerer, J., Sneden, C., Cowan, J. J., Collier, J., Woolf, V. M., & Lawler, J. E. 2004, ApJ, 617, 1091
Smartt, S. J., et al. 2016, MNRAS, 462, 4094
Soares-Santos, M., et al. 2016, ApJ, 823, L33
Tanaka, M. 2016, Advances in Astronomy, 2016, 634197
Tanaka, M., & Hotokezaka, K. 2013, ApJ, 775, 113
Tanaka, M., Hotokezaka, K., Kyutoku, K., Wanajo, S., Kiuchi, K., Sekiguchi, Y., & Shibata, M. 2014, ApJ, 780, 31
Tanvir, N. R., Levan, A. J., Fruchter, A. S., Hjorth, J., Hounsell, R. A., Wiersema, K., & Tunnicliffe, R. L. 2013, Nature, 500, 547
Wanajo, S., & Janka, H.-T. 2012, ApJ, 746, 180
Wanajo, S., Sekiguchi, Y., Nishimura, N., Kiuchi, K., Kyutoku, K., & Shibata, M. 2014, ApJ, 789, L39
Wollaeger, R. T., et al. 2017, arXiv:1705.07084
Wu, M.-R., Fernández, R., Martínez-Pinedo, G., & Metzger, B. D. 2016, MNRAS, 463, 2323
Yang, B., et al. 2015, Nature Communications, 6, 7323
Yoshida, M., et al. 2017, PASJ, 69, 9